Journal of Advanced Research 28 (2021) 43–49

Contents lists available at ScienceDirect

Journal of Advanced Research

journal homepage: www.elsevier.com/locate/jare

Nodal ring spin gapless semiconductor: New member of spintronic materials

Tie Yang [a], Zhenxiang Cheng [b,*], Xiaotian Wang [a,*], Xiao-Lin Wang [b]

[a] School of Physical Science and Technology, Southwest University, Chongqing 400715, China
[b] Institute for Superconducting and Electronic Materials, University of Wollongong, Wollongong 2500, Australia

HIGHLIGHTS

- Innumerable spin gapless points identified in the stable materials Mg_2VO_4.
- Multiple nodal rings located exactly at Fermi level with all hourglass shape dispersions.
- Very clean spin gapless band structures and nodal ring states with no other band interferences.
- Strong robustness against both the spin orbit coupling effect and strain conditions.
- A novel concept of nodal ring spin gapless semiconductor is defined.

GRAPHICAL ABSTRACT

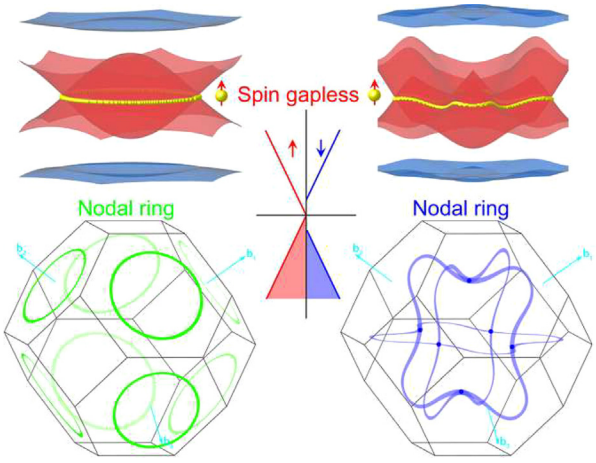

ARTICLE INFO

Article history:
Received 4 May 2020
Revised 1 June 2020
Accepted 20 June 2020
Available online 23 June 2020

ABSTRACT

Introduction: Spin gapless semiconductors (SGSs) and nodal ring states (NRSs) have aroused great scientific interest in recent years due to their unique electronic properties and high application potential in the field of spintronics and magnetoelectronics.
Objectives: Since their advent, all SGSs and NRSs have been predicted in independent materials. In this work, we proposed a novel type of material, nodal ring spin gapless semiconductor (NRSGS), which combines both states of the SGSs and NRSs.
Methods: The synthesized material Mg_2VO_4 has been detailed with band structure analysis based on first principle calculations.
Results: Obtained results revealed that there are gapless crossings in the spin-up direction, which are from multiple topological nodal rings located exactly at the Fermi energy level. Mg_2VO_4 combines the advantages inherited from both NRSs and SGSs in terms of the innumerable gapless points along multiple nodal rings with all linear dispersions and direct contacts. In addition, Mg_2VO_4 also shows strong robustness against both the spin orbit coupling effect and strain conditions.
Conclusion: For the first time, we propose the concept of an NRSGS, and the first such material candidate Mg2VO4 can immediately advance corresponding experimental measurements and even facilitate real applications.

Peer review under responsibility of Cairo University.
* Corresponding authors.
E-mail addresses: cheng@uow.edu.au (Z. Cheng), xiaotianwang@swu.edu.cn (X. Wang).

https://doi.org/10.1016/j.jare.2020.06.016
2090-1232/

Introduction

In recent years, spin gapless semiconductors (SGSs) and nodal ring states (NRSs) have attracted tremendous research interest in the condensed matter physics community due to their unique electronic band structures [1–26]. For SGSs, a gap is present in one spin channel, whereas the valence band maximum touches the conduction band minimum exactly at the Fermi level in the other spin channel, forming a gapless contact. The left panel of Fig. 1 shows all the different types of SGSs. Due to these unique band structures, SGSs have several interesting properties [27]: zero energy consumption for electron excitation from the valence band to the conduction band; very high electron mobility; and full spin polarization of both electron and hole charge carriers. Thus, SGSs have very promising applications in the fields of magnetoelectronics and spintronics [4,6,7,28]. For NRSs, topologically protected and symmetrically defined nontrivial linear band crossings are formed by the valence bands and conduction bands near the Fermi level [29,30]. These topological nodal states can induce very fascinating phenomena in general relativity and high energy physics beyond condensed matter physics, for example, artificial white/black holes, gravitational lenses [31] and chiral anomalies [32]. Nodal rings are characterized by closed nodal loops in the Brillouin zone, and several typical nodal ring types are displayed in the right panel of Fig. 1.

Since their advent, many SGSs and NRSs have been theoretically predicted in both 2D and 3D materials, and a few of them have been experimentally synthesized. However, as of now, the studies on the two material states are all independent. Thus, a simple question arises: *is it possible to have these two properties together in a single material?* With this idea in mind, we proposed a novel type of material, a nodal ring spin gapless semiconductor, which combines the characteristics of both SGSs and NRSs in one material, i.e., the nodal ring state is present only in one spin channel with its linear crossing points exactly along the Fermi energy level. Since NRSs have been reported in magnetic materials much less compared with the nonmagnetic counterparts, the spin gapless feature even further narrows down the possible material. We have found one synthesized bulk material, Mg_2VO_4 [33], as a potential candidate, and first principles calculations prove that it manifests both the spin gapless semiconducting property and nodal ring states. Furthermore, Mg_2VO_4 as an NRSGS exhibits multiple advantages: (1) innumerable gapless band crossing points along multiple nodal rings; (2) all nodal rings with hourglass shape dispersions, which render the gapless crossings all linear dispersions and direct contacts; (3) very clean spin gapless band structures and nodal ring states with no other band interferences; (4) strong robustness against both the spin orbit coupling effect and strain conditions. Therefore, Mg_2VO_4 can serve as a promising material platform for further studying the spin gapless semiconducting behaviour and topological nodal ring states and can immediately advance corresponding experimental measurements.

Computational methods

We performed first principles calculations with the Vienna Ab initio Simulation Package [34,35] (VASP) based on density functional theory [36]. The projector augmented wave (PAW) method [37] is applied for the ionic potentials, and the Perdew-Burke-Ernzerhof (PBE) functional [38] within the generalized gradient approximation [39] (GGA) is selected for the exchange–correlation potential. After an initial convergence test, a cut-off energy of 520 eV is selected for the plane-wave basis set, and a *k* point mesh of a 12 × 12 × 12 Monkhorst-Pack grid is employed for the Brillouin zone sampling. The structure relaxation is reached until the residual force is less than 0.001 eV/Å, and the self-consistent field iteration convergence tolerance is set as a total energy difference less than 1×10^{-6} eV. The DFT + U method [40] and the nonlocal Heyd-Scuseria-Ernzerhof (HSE06) functional [41] have also been utilized to further verify the electronic properties.

Results and discussions

The bulk material Mg_2VO_4 has been experimentally synthesized [33] and it is confirmed to adopt a cubic structure with space group $Fm\bar{3}m$ (No. 227). Fig. 2 a) displays the primitive cell of Mg_2VO_4 with 14 atoms, including 4 Mg, 8O and 2 V. The two V atoms are located in the centre of two tetrahedrons formed by O atoms. To obtain the ground state of Mg_2VO_4 and also obtain the lattice parameters, three magnetic arrangements have been considered: the nonmagnetic (NM), ferromagnetic (FM) and antiferromagnetic (AFM) states. In addition, to better describe the strong correlation effect for the d electrons of V atoms, the DFT + U method is also used with different Hubbard U values considered. The calculated total energies and lattice constants are shown in Fig. 2 c). It is clearly seen that the ferromagnetic state has the lowest energy throughout the entire Hubbard U value scan, indicating that it is

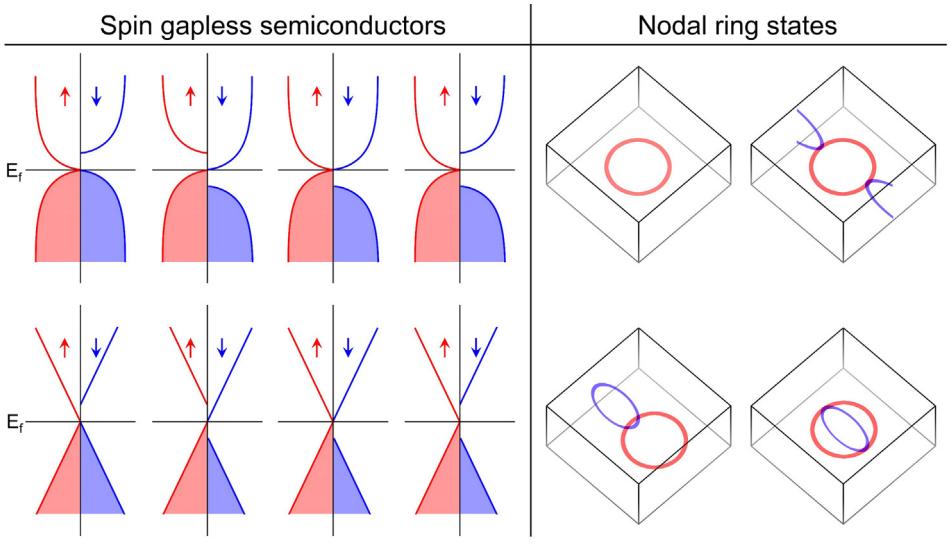

Fig. 1. Different types of spin gapless semiconductors (left) and nodal ring states (right).

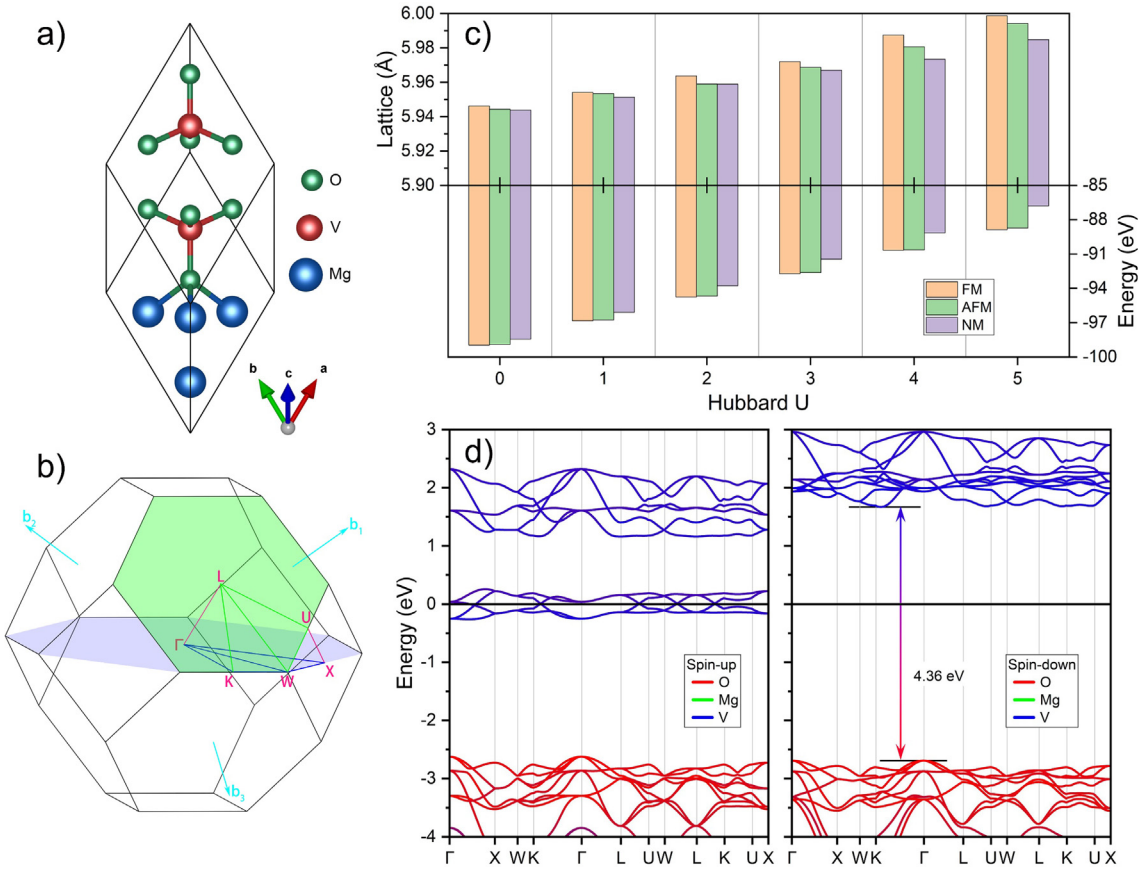

Fig. 2. Crystal structure of Mg_2VO_4 in terms of the primitive cell (a) and the first bulk Brillouin zone with high symmetry points and paths. Calculated lattice constants and total energies (c) for the ferromagnetic (FM), antiferromagnetic (AFM) and nonmagnetic (NM) states under different Hubbard U values. Electronic band structures (d) of the two spin channels along with atomic projections.

energetically more favourable as the ground state. The obtained lattice constants slightly increase with U simply because of the stronger on-site Coulomb repulsion introduced at higher U values. Overall, the optimized lattice parameters under different U values have a very small variation (<1%) and match the experimental values (a = b = c = 5.931 Å) very well.

Based on the obtained lattice parameters and magnetic ground state of Mg_2VO_4, we can further examine its electronic properties. The electronic band structures have been calculated under different U values and are further examined through the Heyd-Scuseria-Ernzerhof (HSE06) functional. It is found that the result at U = 2 agrees well with the HSE06 calculation (see Fig. S1 in the supplementary material), and thus, we use it for the following discussions. The spin-polarized electronic band structure is displayed in Fig. 2 d) along with element projections, and the corresponding high symmetry points and paths are plotted within the first Brillouin zone in Fig. 2 b). It should be noted that the spin orbit coupling (SOC) effect has not been considered here because mainly light elements are involved, and it will be discussed later. From the band structure, the following features can be clearly observed: (i) There are bands crossing at the Fermi level in the spin-up direction, while a large gap of 4.36 eV is present in the spin-down channel. (ii) The bands near the Fermi energy level are mainly contributed by the V and O elements, and in particular, the bands crossing the Fermi level in the spin-up channel are only from V. (iii) There are several linear band crossings in the spin-up channel, and the crossing points are all located at the Fermi level. (iv) The crossing bands near the Fermi level in the spin-up direction are well separated from other bands both above and below them.

Following the above discussion, we found that Mg_2VO_4 belongs to the family of spin gapless semiconductors with a linear dispersion between the energy and momentum [42]. Compared with other SGSs reported thus far [3,4,7,43,44], Mg_2VO_4 has multiple advantages: (i) it is one of the experimentally synthesized SGSs containing mostly light elements; (ii) it has much more gapless points present than other SGSs; (iii) all crossing points have a linear dispersion; (iv) the energy band structures for the SGS behaviour are very clean in the sense that there are no other band interferences. To better understand the origin of the gapless bands, we plot the band dispersion of the spin-up channel around the Fermi energy level in Fig. S1. Since the V atom mostly contributes to this area, we further decompose the bands into orbital projections, and only the components of the *d* orbitals are considered because the contributions of the *s* and *p* orbitals are negligible. The projection weight is proportional to the coloured line width, and it is found that all the gapless crossings are mainly formed by the d_{xz} and d_{yz} orbitals of V atoms.

According to the locations of the gapless crossing points, they can be divided into two groups: one in the Γ-K-W-X plane, see the blue shaded area in Fig. 2 b), which we name the Γ plane, and the other one in the L-K-W-U plane, see the green shaded area in Fig. 2 b), which we name the L plane. Let us first consider the three crossing points in the L plane: the first one is along the L-U path; the second one is along the L-K path; and the third one is along the L-W path. The former two crossing points have the same distance from the L point. Since all these three points are located in the same plane and formed by the same two bands, we speculate that they are not isolated. To confirm this and obtain a clear idea

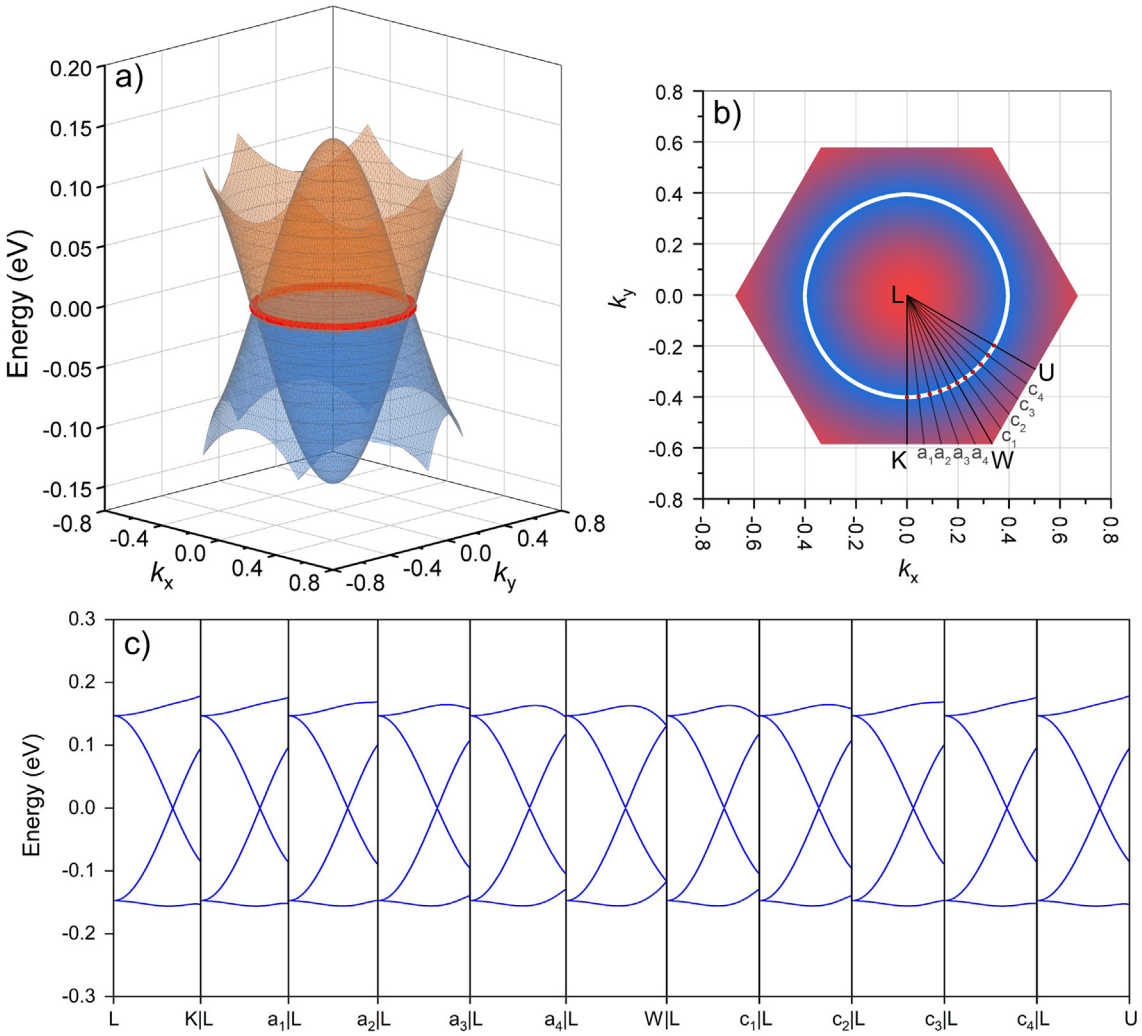

Fig. 3. Calculated three-dimensional energy band dispersion in the L plane (a). The transparent red mesh represents the conduction band dispersion, and the blue mesh represents for the valence band dispersion, with crossing points highlighted by red dots. (b) Top view of the conduction band projection, with the white line indicating the crossing ring position and the high symmetry points and paths overlaid. (c) High precision band dispersion scan along the evenly distributed path segments taken in (b). (For interpretation of the references to color in this figure legend, the reader is referred to the web version of this article.)

of their formation, we have performed a full scan of the energy bands for the entire area in the L plane, and the calculated band dispersion is shown in Fig. 3. The conduction band dispersion surface touches the valence band dispersion surface exactly at the Fermi energy level, see the corresponding half transparent red and blue mesh surfaces in Fig. 3 a), and the crossing points form a closed ring. The hexagonal coloured area in Fig. 3 b) corresponds to the projection of the conduction band dispersion, with the gapless crossing points highlighted by the white line. To have a better visualization, high symmetry points are also indicated. It is observed that the gapless points indeed form a perfect circle with the L point as its centre. Actually, this circle formed by the linear gapless crossing corresponds to a nodal ring in topological material [8,11,14,17,19,21–25,45–47]. It should be mentioned here that there is generally a finite energy variation along a nodal ring, and thus, we further examine the energy dispersion with very high precision along several path segments among the L-K, L-W and L-U paths, as indicated by the black lines in Fig. 3 b). The calculated band dispersions are accordingly shown in Fig. 3 c), and we can see that all the gapless dispersions have a linear fashion and that the crossing points are exactly at the Fermi level. The crossing points are also marked as red dots in the original paths in Fig. 3 a), and their connections indeed form one-sixth of a full circle. Consequently, it is confirmed that the gapless points in the L plane are formed by the same band dispersion and that they form a nodal ring located at the Fermi energy level. Moreover, it should be noted that all the gapless band crossing points in the L plane enjoy an hourglass type dispersion in the energy range from −0.1 to 0.1 eV, similar to $Ni_2C_{24}S_6H_{12}$ [48] and ReO_2 [9].

Similarly, we now turn to the two gapless points in the Γ plane: the first one is along the Γ-X path, and the second one is along the Γ-K path, as shown in Fig. 2 d). To determine their formation mechanism, we have also performed a full scan in the Γ plane, and the obtained band dispersion is shown in Fig. 4 a). The conduction band dispersion contacts the valence band dispersion at the Fermi level, and they also form a closed ring. Different from the circular shape found in the L plane, the ring in the Γ plane has the shape of a rounded quadrangular star, as highlighted by the white color line in Fig. 4 b). Similarly, this ring is also a topological nodal ring, and the two gapless points actually correspond to only two points along the line. According to this line, there should be another gapless point along the Γ-W path. To confirm this and also check the energy variation of the gapless line, we further calculated the energy dispersions along several segment paths,

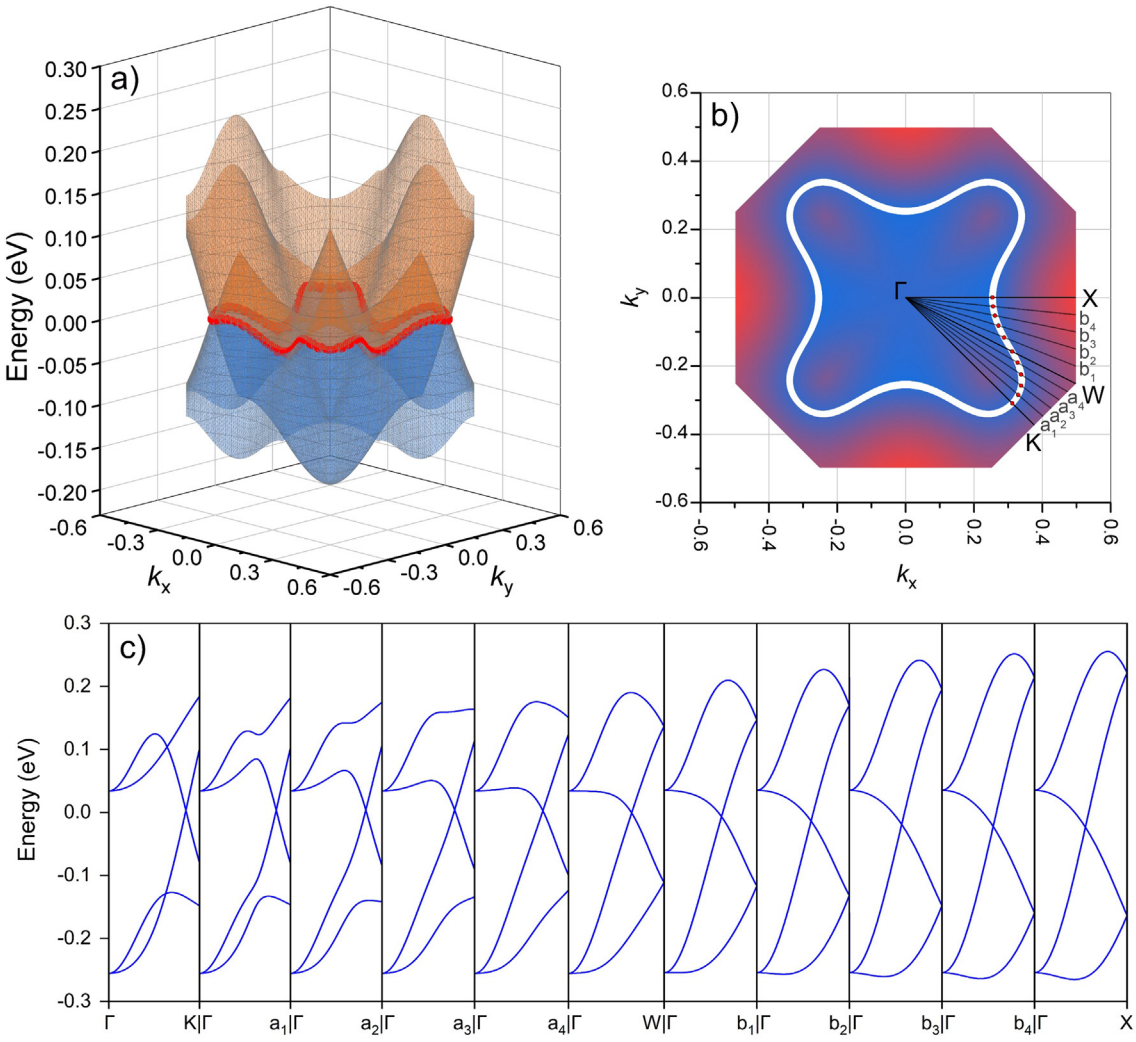

Fig. 4. Calculated three-dimensional energy band dispersion in the Γ plane (a). The transparent red mesh represents the conduction band dispersion, and the blue mesh represents the valence band dispersion, with crossing points highlighted by red dots. (b) Top view of the conduction band projection, with the white line indicating the crossing ring position and the high symmetry points and paths overlaid. (c) High precision band dispersion scan along the evenly distributed path segments taken in (b). (For interpretation of the references to color in this figure legend, the reader is referred to the web version of this article.)

see Fig. 4 b). The corresponding band shapes are displayed in Fig. 4 c), and we can clearly see that all the crossing points are at the Fermi energy level. The gapless point connections form one-eighth of the entire ring, as shown in Fig. 4 b). Thus, it is also confirmed that the gapless points in the Γ plane are from the same band dispersion and that they form a topological ring with the shape of a rounded quadrangular star. In a smaller energy range, the gapless band crossings also exhibit an hourglass type dispersion.

Based on the symmetry of the lattice cell and its reciprocal space, the gapless nodal rings should have counterparts in other symmetrical planes. A careful scan was performed in the entire Brillouin zone, and all the gapless lines were identified and are plotted in Fig. S3. There are two other planes symmetrical to the Γ plane in the vertical direction, and nodal rings have also been found, see Fig. S3 a). For the L plane, there are seven other symmetrical planes (they compose all the eight hexagonal areas on the surface of the Brillouin zone), and nodal rings have all been found, see Fig. S3 b). Not only are the shapes of the nodal rings distinct from those of these two symmetrical plane systems, but also, their locations are also very different: the three blue lines are all inside the Brillouin zone, and more interestingly, there are six intersection points in total between each two of them; the eight circles are all on the surface, and they are all symmetrical between each other. All the points along the nodal rings have double degeneracy except the six intersection points with fourfold degeneracy. The former double degenerate lines correspond to the Weyl nodal rings, and the other six fourfold degenerate points form the Dirac nodal points.

As previously mentioned, Mg_2VO_4 contains mostly light elements, and the SOC strength is expected to be relatively weak. This can be assessed by the electronic band structure calculated with the SOC effect. As shown in Fig. S4, all the gapless points have been opened up under the consideration of the SOC effect, which is very common for most nodal ring topological materials [45,49,50]. However, all the gaps are very small, actually much smaller than the most of those for the known nodal ring materials; therefore, the SOC effect in the current material can be safely neglected. In addition, strain conditions are also considered because they often occur during material preparation and processing and are even frequently used for structural engineering, such as thin film epitaxy and heterojunction combination. This would also have an impact on the electronic properties, particularly the spin gapless feature and nodal ring states. Thus, we have also evaluated the structural

strain effects on the electronic band structures of Mg_2VO_4 by simply applying uniform hydrostatic pressure on the materials. The obtained results are reported in Fig. S5, and it is found that the energy bands have almost no variation and that the spin gapless behaviour and nodal ring states are well maintained under the currently studied pressure range from 1 to 3 GPa. Finally, we investigated the dynamic and mechanical stabilities of Mg_2VO_4 with DFT calculations, and detailed results are included in the supplementary material. It is verified that Mg_2VO_4 is both dynamically and mechanically stable. Several mechanical parameters have been computed, and their direction dependences have been assessed, which clearly reveal that Mg_2VO_4 has relatively small mechanical anisotropy. This could be quite important for practical applications in different device structures, such as heterojunction formation.

Conclusion

In this work, we have proposed a new concept of an NRSGS, which combines characteristics inherited from both NRSs and SGSs. Mg_2VO_4 is selected as the first candidate material. First principles calculation results revealed that this material has a ferromagnetic ground state, and the obtained lattice parameters match the experimental measurements very well. The spin-polarized band structures characterize it into the family of spin gapless semiconductors: there are multiple gapless points present in the spin-up channel, whereas a very large energy gap of 4.36 eV exists in the spin-down channel. A full scan of the energy dispersion in the Brillouin zone was performed, and it has been found that the gapless points are from multiple topological nodal rings. Thus, Mg_2VO_4 can be regarded as a new member of spintronic materials, nodal ring spin gapless semiconductor, and it can combine the advantages of the two material types together: innumerable gapless crossing points along multiple nodal rings; hourglass shape dispersions for all nodal rings, which render the gapless crossings all linear dispersions and direct contacts; very clean spin gapless band structures and nodal ring states with no other band interferences. The spin orbit coupling effect was further examined, and it has a negligible impact on the spin gapless nature and nodal ring states because this material has mostly light elements. Strain conditions were considered, and it has been found that the gapless behaviour is very robust against uniform hydrostatic pressure in the studied range. Finally, the mechanical and dynamic stabilities of Mg_2VO_4 were also confirmed, and the directional dependences revealed that Mg_2VO_4 has relatively small mechanical anisotropy, which is very suitable for the formation of different device structures. Overall, the currently presented nodal ring spin gapless semiconductor Mg_2VO_4 has already been synthesized and can immediately inspire corresponding experimental measurements. Moreover, since there a variety of nodal ring shapes in topological materials, we expected new topological nodal ring spin gapless materials to be found with the increasing scientific interest and expanding research effort.

Compliance with ethics requirements

This article does not contain any studies with human or animal subjects.

Declaration of Competing Interest

The authors declare that they have no known competing financial interests or personal relationships that could have appeared to influence the work reported in this paper.

Acknowledgments

This work was supported by National Natural Science Foundation of China [61904153].

Appendix A. Supplementary material

Supplementary data to this article can be found online at https://doi.org/10.1016/j.jare.2020.06.016.

References

[1] Bainsla L, Mallick AI, Raja MM, Coelho AA, Nigam AK, Johnson DD, et al. Origin of spin gapless semiconductor behavior in CoFeCrGa: Theory and experiment. Phys Rev B 2015;92:045201.
[2] Deng YX, Chen SZ, Zeng Y, Feng YX, Zhou WX, Tang LM, et al. Spin gapless semiconductor and half-metal properties in magnetic penta-hexa-graphene nanotubes. Org Electron 2018;63:310–7.
[3] Gao G, Ding G, Li J, Yao K, Wu M, Qian M. Monolayer MXenes: promising half-metals and spin gapless semiconductors. Nanoscale 2016;8:8986–94.
[4] Li X, Yang J. First-principles design of spintronics materials. Natl Sci Rev 2016;3:365–81.
[5] Manna K, Sun Y, Muechler L, Kubler J, Felser C. Heusler, weyl and berry. Nat Rev Mater 2018;3:244–56.
[6] Wang XT, Cheng ZX, Wang JL, Wang XL, Liu GD. Recent advances in the Heusler based spin-gapless semiconductors. J Mater Chem C 2016;4:7176–92.
[7] Wang XT, Li TZ, Cheng ZX, Wang XL, Chen H. Recent advances in Dirac spin-gapless semiconductors. Appl Phys Rev 2018;5:041103.
[8] Wang Shan-Shan WW-K, Sheng-Yuan Yang. Progress on topological nodal line and nodal surface. Acta Phys Sin 2019;68. 227101.
[9] Wang S-S, Liu Y, Yu Z-M, Sheng X-L, Yang SA. Hourglass Dirac chain metal in rhenium dioxide. Nat Commun 2017;8:1844.
[10] Wang S-S, Yu Z-M, Liu Y, Jiao Y, Guan S, Sheng X-L, et al. Two-dimensional nodal-loop half-metal in monolayer MnN. Phys Rev Mater 2019;3:084201.
[11] Wang X, Ding G, Cheng Z, Surucu G, Wang X-L, Yang T. Novel topological nodal lines and exotic drum-head-like surface states in synthesized CsCl-type binary alloy TiOs. J Adv Res 2020;22:137–44.
[12] Wang X, Ding G, Cheng Z, Surucu G, Wang X-L, Yang T. Rich topological nodal line bulk states together with drum-head-like surface states in NaAlGe with anti-PbFCl type structure. J Adv Res 2020;23:95–100.
[13] Chen D-Y, Wu Y, Jin L, Li Y, Wang X, Duan J, et al. Superconducting properties in a candidate topological nodal line semimetal SnTaS2 with a centrosymmetric crystal structure. Phys Rev B 2019;100. 064516.
[14] He T, Zhang X, Meng W, Jin L, Dai X, Liu G. Topological nodal lines and nodal points in the antiferromagnetic material β-Fe2PO5. J Mater Chem C 2019;7:12657–63.
[15] Jin L, Zhang X, He T, Meng W, Dai X, Liu G. Topological nodal line state in superconducting NaAlSi compound. J Mater Chem C 2019;7:10694–9.
[16] Li S, Yu Z-M, Liu Y, Guan S, Wang S-S, Zhang X, et al. Type-II nodal loops: Theory and material realization. Phys Rev B 2017;96:081106.
[17] Liu G, Jin L, Dai X, Chen G, Zhang X. Topological phase with a critical-type nodal line state in intermetallic CaPd. Phys Rev B 2018;98:075157.
[18] Fang C, Chen Y, Kee H-Y, Fu L. Topological nodal line semimetals with and without spin-orbital coupling. Phys Rev B 2015;92:081201.
[19] Huang H, Liu J, Vanderbilt D, Duan W. Topological nodal-line semimetals in alkaline-earth stannides, germanides and silicides. Phys Rev B 2016;93.
[20] Bian G, Chang T-R, Sankar R, Xu S-Y, Zheng H, Neupert T, et al. Topological nodal-line fermions in spin-orbit metal PbTaSe2. Nat Commun 2016;7:10556.
[21] Gan LY, Wang R, Jin YJ, Ling DB, Zhao JZ, Xu WP, et al. Emergence of topological nodal loops in alkaline-earth hexaborides XB6 (X = Ca, Sr, and Ba) under pressure. PCCP 2017;19:8210–5.
[22] Zhang X, Jin L, Dai X, Liu G. Highly anisotropic type-II nodal line state in pure titanium metal. Appl Phys Lett 2018;112:122403.
[23] Li S, Liu Y, Wang S-S, Yu Z-M, Guan S, Sheng X-L, et al. Nonsymmorphic-symmetry-protected hourglass Dirac loop, nodal line, and Dirac point in bulk and monolayer X3SiTe6 (X = Ta, Nb). Phys Rev B 2018;97:045131.
[24] Shao D-F, Gurung G, Zhang S-H, Tsymbal EY. Dirac nodal line metal for topological antiferromagnetic spintronics. Phys Rev Lett 2019;122:077203.
[25] Jin L, Zhang XM, Dai XF, Wang LY, Liu HY, Liu GD. Screening topological materials with a CsCl-type structure in crystallographic databases. IUCrJ 2019;6:688–94.
[26] Zhang T-T, Yu Z-M, Guo W, Shi D, Zhang G, Yao Y. From type-II triply degenerate nodal points and three-band nodal rings to type-II dirac points in centrosymmetric zirconium oxide. J Phys Chem Lett 2017;8:5792–7.
[27] Wang XL, Dou SX, Zhang C. Zero-gap materials for future spintronics, electronics and optics. NPG Asia Mater 2010;2:31–8.
[28] Xu GZ, Liu EK, Du Y, Li GJ, Liu GD, Wang WH, et al. A new spin gapless semiconductors family: Quaternary Heusler compounds. Epl-Europhys Lett 2013;102:17007.
[29] Xie LS, Schoop LM, Seibel EM, Gibson QD, Xie W, Cava RJ. A new form of Ca3P2 with a ring of Dirac nodes. Apl Mater 2015;3:083602.

[30] Chen Y, Xie Y, Yang SA, Pan H, Zhang F, Cohen ML, et al. Nanostructured carbon allotropes with weyl-like loops and points. Nano Lett 2015;15:6974–8.
[31] Guan S, Yu Z-M, Liu Y, Liu G-B, Dong L, Lu Y, et al. Artificial gravity field, astrophysical analogues, and topological phase transitions in strained topological semimetals. npj Quantum Mater 2017;2:23.
[32] Son DT, Spivak BZ. Chiral anomaly and classical negative magnetoresistance of Weyl metals. Phys Rev B 2013;88:104412.
[33] Rüdorff W, Reuter B. Die Struktur der Magnesium- und Zink- Vanadinspinelle. Beitrag zur Struktur der Spinelle, Z Anorg Chem 1947;253:194–208.
[34] Kresse G, Joubert D. From ultrasoft pseudopotentials to the projector augmented-wave method. Phys Rev B 1999;59:1758–75.
[35] Hafner J. Ab-initio simulations of materials using VASP: Density-functional theory and beyond. J Comput Chem 2008;29:2044–78.
[36] Payne MC, Teter MP, Allan DC, Arias TA, Joannopoulos JD. Iterative minimization techniques forab initiototal-energy calculations: molecular dynamics and conjugate gradients. Rev Mod Phys 1992;64:1045–97.
[37] Blöchl PE. Projector augmented-wave method. Phys Rev B 1994;50:17953–79.
[38] Ernzerhof M, Scuseria GE. Assessment of the Perdew–Burke–Ernzerhof exchange-correlation functional. J Chem Phys 1999;110:5029–36.
[39] Perdew JP, Burke K, Ernzerhof M. Generalized gradient approximation made simple. Phys Rev Lett 1996;77:3865–8.
[40] Anisimov VI, Zaanen J, Andersen OK. Band theory and mott insulators: hubbard U instead of stoner I. Phys Rev B 1991;44:943–54.
[41] Heyd J, Scuseria GE, Ernzerhof M. Hybrid functionals based on a screened Coulomb potential. J. Chem. Phys. 2003;118:8207–15.
[42] Wang XL. Proposal for a new class of materials: spin gapless semiconductors. Phys Rev Lett 2008;100:156404.
[43] Skaftouros S, Ozdogan K, Sasioglu E, Galanakis I. Search for spin gapless semiconductors: The case of inverse Heusler compounds. Appl Phys Lett 2013;102. 022402.
[44] Ouardi S, Fecher GH, Felser C, Kubler J. Realization of spin gapless semiconductors: the Heusler compound Mn2CoAl. Phys Rev Lett 2013;110. 100401.
[45] Zhang X, Jin L, Dai X, Liu G. Topological type-II nodal line semimetal and dirac semimetal state in stable kagome compound Mg3Bi2. J Phys Chem Lett 2017;8:4814–9.
[46] Shi WJ, Muechler L, Manna K, Zhang Y, Koepernik K, Car R, et al. Prediction of a magnetic Weyl semimetal without spin-orbit coupling and strong anomalous Hall effect in the Heusler compensated ferrimagnet Ti2MnAl. Phys Rev B 2018;97. 060406.
[47] Zhang R-W, Zhang Z, Liu C-C, Yao Y. Nodal line spin-gapless semimetals and high-quality candidate materials. Phys Rev Lett 2020;124. 016402.
[48] Wei L, Zhang X, Zhao M. Spin-polarized Dirac cones and topological nontriviality in a metal–organic framework Ni2C24S6H12. PCCP 2016;18:8059–64.
[49] Zhang XM, Yu ZM, Zhu ZM, Wu WK, Wang SS, Sheng XL, et al. Nodal loop and nodal surface states in the Ti3Al family of materials. Phys Rev B 2018;97. 235150.
[50] Zhang X, Yu Z-M, Sheng X-L, Yang HY, Yang SA. Coexistence of four-band nodal rings and triply degenerate nodal points in centrosymmetric metal diborides. Phys Rev B 2017;95. 235116.